Arctic–North Atlantic Interactions and Multidecadal Variability of the Meridional Overturning Circulation

JOHANN H. JUNGCLAUS AND HELMUTH HAAK

Max Planck Institute for Meteorology, Hamburg, Germany

MOJIB LATIF

Leibniz Institut fuer Meereswissenschaften, Kiel, Germany

UWE MIKOLAJEWICZ

Max Planck Institute for Meteorology, Hamburg, Germany

(Manuscript received 6 August 2004, in final form 20 January 2005)

ABSTRACT

Analyses of a 500-yr control integration with the non-flux-adjusted coupled atmosphere–sea ice–ocean model ECHAM5/Max-Planck-Institute Ocean Model (MPI-OM) show pronounced multidecadal fluctuations of the Atlantic overturning circulation and the associated meridional heat transport. The period of the oscillations is about 70–80 yr. The low-frequency variability of the meridional overturning circulation (MOC) contributes substantially to sea surface temperature and sea ice fluctuations in the North Atlantic. The strength of the overturning circulation is related to the convective activity in the deep-water formation regions, most notably the Labrador Sea, and the time-varying control on the freshwater export from the Arctic to the convection sites modulates the overturning circulation. The variability is sustained by an interplay between the storage and release of freshwater from the central Arctic and circulation changes in the Nordic Seas that are caused by variations in the Atlantic heat and salt transport. The relatively high resolution in the deep-water formation region and the Arctic Ocean suggests that a better representation of convective and frontal processes not only leads to an improvement in the mean state but also introduces new mechanisms determining multidecadal variability in large-scale ocean circulation.

1. Introduction

The interdecadal variability of the climate system has received increasing attention in recent years. A proper estimate of the natural fluctuations of the climate system is crucial for the detection of anthropogenic climate change. This holds in particular for variations at the decadal to centennial time scales at which man's impact on climate is most likely to occur (e.g., Houghton et al. 2001).

The observational record of Northern Hemisphere temperature and North Atlantic sea surface temperature (SST) has been extended during the last decade (e.g., Mann et al. 1998, 1999) to cover the last few centuries. Mann et al. (1998) demonstrate that the Northern Hemisphere temperature time series exhibits fluctuations with periods of about 50–100 yr. Similar variations can be found in the North Atlantic SST dataset produced by the Hadley Centre (e.g., Folland et al. 1999). Short-term (interannual to decadal) variations are driven primarily by the atmosphere and can be characterized by the "tripole" pattern of SSTs that is driven by heat flux anomalies associated with the variations of the North Atlantic Oscillation (NAO; e.g., Wu and Gordon 2002). At longer time scales, however, the SST anomaly pattern is characterized by a more homogeneous pattern with anomalies of one sign in the North Atlantic and of opposite sign south of the equator (e.g., Folland et al. 1984; Delworth and Mann 2000).

Simulations with coupled atmosphere–ocean general circulation models (CGCMs) have linked these mul-

Corresponding author address: Dr. Johann H. Jungclaus, Max Planck Institute for Meteorology, Bundesstrasse 53, 20146 Hamburg, Germany.
E-mail: jungclaus@dkrz.de

tidecadal fluctuations to variations in the large-scale meridional overturning circulation (MOC; Delworth et al. 1993, hereafter DMS93; Timmermann et al. 1998; Delworth and Mann 2000). MOC fluctuations go along with changes in the northward heat transport influencing the SST and sea surface salinity (SSS) in the North Atlantic. Delworth and Mann (2000) describe a 50–70-yr mode in the Geophysical Fluid Dynamics Laboratory (GFDL) model that shows some consistency with observed SST fluctuations. The mechanisms behind the 30–35-yr (Timmermann et al. 1998) and the 50–70-yr (DMS93; Delworth and Mann 2000) modes show some similarities but differ in one important aspect. Whereas the MOC variability in the GFDL model is interpreted to represent an ocean-only mode that is excited by atmospheric noise (Griffies and Tziperman 1995; Delworth and Greatbatch 2000), Timmermann et al. (1998) point to the importance of two-way interactions between the ocean and the atmosphere and postulate the existence of a coupled mode.

A common feature of the multicentury integrations is that the key factor determining the strength of the overturning is the density in the deep-water formation regions. DMS93 show that large-scale salinity anomalies are transported into the convection region south of Greenland by the subpolar gyre. In a later article, the same authors (Delworth et al. 1997) describe also an important freshwater contribution originating in the Arctic Ocean; this finding is of particular relevance to our present paper. In the coupled mode identified by Timmermann et al. (1998), the thermohaline circulation (THC) variability influences the atmospheric pressure patterns over the North Atlantic, in particular the NAO. This, in turn, leads to anomalous freshwater input and surface density anomalies in the convection regions.

Delworth and Greatbatch (2000) reviewed the interdecadal mode in the GFDL coupled model and found that the variability vanishes under climatological surface fluxes (calculated from the fully coupled experiment and applied to the stand-alone ocean model) but reappears when random time series of the coupled simulation heat fluxes are used. They conclude that the oscillations are to be interpreted as damped oscillations excited by stochastic atmospheric forcing.

Using highly idealized models of the Atlantic (ATL) circulation, Huck et al. (1999, 2001) and Te Raa and Dijkstra (2002, 2003) find intrinsic modes of decadal to interdecadal MOC variability in simulations with fixed surface fluxes and simplified atmosphere models. The authors conclude that the oscillation is caused by a phase difference between changes in the meridional heat transport and a zonal redistribution of density anomalies.

The horizontal redistribution of density anomalies involves both temperature and salinity. The convectively active regions in the Greenland–Iceland–Norwegian (GIN) Seas and the Labrador Sea (LS) are influenced by lateral transports from the Atlantic (warm, saline) and Arctic (cold, fresh) domain. In particular, variations in the high northern latitude freshwater budget are expected to affect the formation of North Atlantic Deep Water (NADW; e.g., Broecker 1997). Freshwater sensitivity experiments with uncoupled (e.g., Maier-Reimer and Mikolajewicz 1989) and coupled GCMs (e.g., Schiller et al. 1997) show that NADW formation and, subsequently, the meridional overturning circulation cannot be sustained when too much freshwater is added to the system. Even relatively small freshwater anomalies that are related to the so-called "Great Salinity Anomalies" in the North Atlantic (Dickson et al. 1988; Belkin et al. 1998) can regionally and temporarily reduce the convection in the Labrador Sea (Curry et al. 1998). Their influence on the strength of the thermohaline circulation is, however, under debate (Curry and McCartney 2001; Häkkinen 1999; Haak et al. 2003).

A clear advantage of the model presented here compared with the previous generation of climate models is that no flux adjustment had to be applied to maintain a reasonably stable climate. The need for flux adjustments reflects incompatible transport divergences in model ocean and model atmosphere. Marotzke and Stone (1995) showed that the erroneous transports and fluxes are related to erroneous feedbacks, that is, even though the fluxes are "corrected," the feedbacks remain incorrect.

The model offers considerably higher resolution in the deep-water formation regions and in the Nordic Seas/Arctic Ocean than previous models that were used for multicentury, large-scale integrations. Given the importance of ocean convection and related processes, such as the overflows, in controlling the overturning circulation, we wish to investigate if a better representation of these processes leads to the identification of a new feedback mechanism determining low-frequency variability in the ocean.

The paper is organized as follows. A description of the coupled model and its components is given in section 2 together with a discussion of the mean state. Section 3 describes the multidecadal variability of the MOC, the oceanic heat transports, and related variables. Regression analysis is applied to various model fields to identify the relevant feedbacks producing the multidecadal variations. Section 4 includes further dis-

cussion of the results and a comparison with observations.

2. The model

The model used here is the Max-Planck-Institute for Meteorology global atmosphere–ocean–sea ice model: cycle 5.02 of the atmosphere European Centre for Medium-Range Weather Forecasts (ECMWF) Hamburg Model/Max-Planck-Institute Ocean Model (ECHAM5/MPI-OM). A thorough description of the atmosphere model and the novel features (compared to previous versions) is beyond the scope of this paper and is given in a technical report by Roeckner et al. (2003). Land surface processes are simulated with an imbedded simplified land surface module (Schulz et al. 2001). In the present study, the atmosphere model is run at a spectral T42 (~2.8°) resolution with 19 vertical layers.

The ocean model MPI-OM (Marsland et al. 2003) is formulated on the horizontal Arakawa C grid and uses geopotential vertical coordinates with partial cells in the vertical. Tracer advection is computed with a second-order total variation diminishing scheme (Sweby 1984). The along-isopycnal diffusion is implemented following Griffies (1998). The effect of horizontal tracer mixing by advection with the unresolved eddies is parameterized following Gent et al. (1995). For the vertical eddy viscosity and diffusion, the Richardson-number-dependent scheme of Pacanowski and Philander (1981, hereafter PP) is applied. Since the PP scheme in its classical form underestimates the turbulent mixing close to the surface, an additional wind mixing parameterization is included. The wind stirring near the surface is proportional to the cube of the 10-m wind speed and decays exponentially with depth.

In the presence of static instability, convective overturning is parameterized by greatly enhanced vertical diffusion. A slope convection scheme has been included that allows for a better representation of the flow of statically unstable dense water over sills and off shelves (see Marsland et al. 2003 for details).

In the experiment analyzed here, we use the same curvilinear grid setup as in Marsland et al. (2003, their Fig. 1). To avoid the singularity at the North Pole, the grid poles are located at 80°N, 30°W (northern Greenland) and 80°S, 30°W (Antarctica, close to Weddell Sea), respectively. The symmetry about the equator allows for an additional refinement of the grid between 10°S and 10°N where the meridional resolution is gradually increased to 0.5°. Another advantage of the placement of the grid poles is a relatively high resolution in the deep-water formation regions of the Greenland Sea (GS), the Labrador Sea, and the Weddell Sea. The grid has a nominal resolution of 2.8°, and the actual resolution varies from about 10 km near Greenland and the Weddell Sea to more than 300 km in the Pacific. A dynamic–thermodynamic Hibler-type (Hibler 1979) sea ice model is embedded in the ocean model code (see Marsland et al. 2003 for details). The atmosphere and the sea ice–ocean models are coupled by means of the Ocean Atmosphere Sea Ice Soil (OASIS) coupler (Terray et al. 1998). The fluxes of momentum, heat, and freshwater are transferred from the atmosphere to the coupler, which also performs the interpolation onto the ocean grid. The ocean fields given to the atmosphere via the coupler are SST, ice thickness and concentration, and snow thickness. River runoff and glacier calving are treated interactively, and the respective freshwater is transferred to the ocean together with the atmospheric precipitation field.

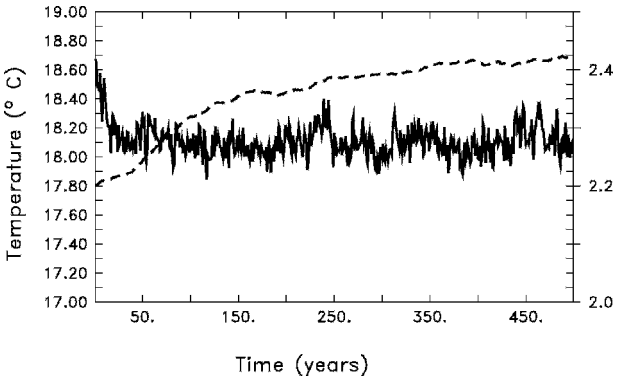

FIG. 1. Evolution of globally averaged temperature near the surface at 10-m depth (solid line) and in the deep ocean at 2500-m depth (dashed line; right axis).

The initial fields for the ocean are taken from the output of model year 150 of the climatologically forced experiment described in Marsland et al. (2003). This uncoupled run was initialized with temperature and salinity data from the *World Ocean Atlas 1998* (Levitus et al. 1998). The atmospheric forcing was derived from the ECMWF reanalysis and is documented by Röske (2001).

Once coupled, the ocean model state is not in balance with the fluxes. Globally averaged SST time series (Fig. 1) show a cooling by about 0.5 K over the first 15 yr but remain stable for the rest of the experiment. Too-cold temperatures occur in the equatorial Pacific; a problem that is common to large-scale OGCMs and is often referred to as "equatorial cold bias." In the deep ocean, the adjustment is slower, but the temperature almost equilibrates after 100–200 yr (Fig. 1). Overall the horizontally averaged temperature remains close to the initial values (Fig. 2a) with a small warming trend in the deep ocean. The salinity field, however, exhibits considerable drift. The major part of the drift in the depth

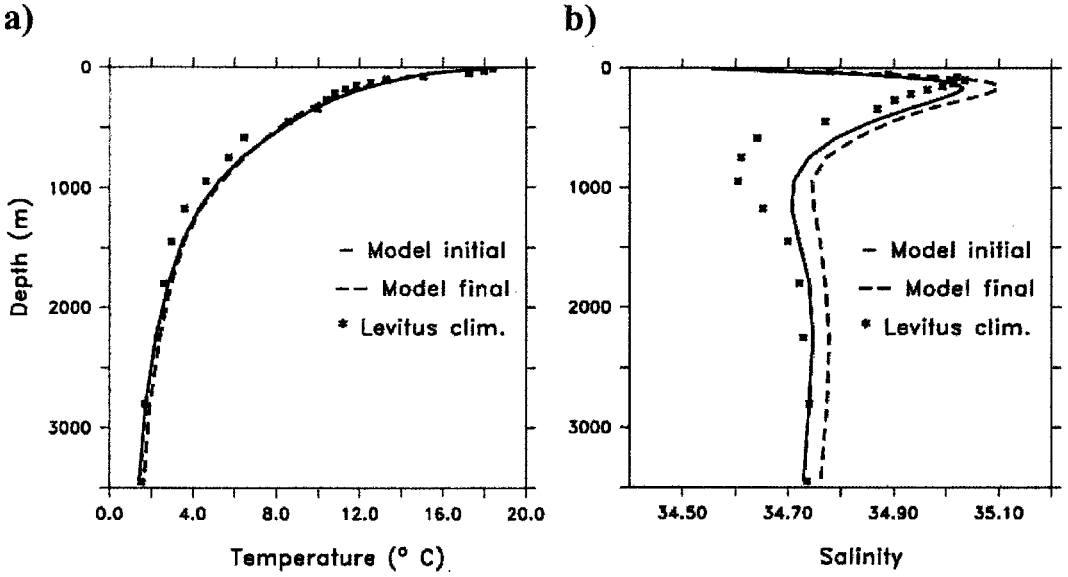

FIG. 2. Globally averaged (a) temperature and (b) salinity. Symbols represent the profiles at the start of the uncoupled spinup run (Levitus et al. 1998), solid lines are the profiles at the beginning of the coupled experiment, and the dashed lines are the profiles at the end of the coupled experiment (averaged over the years 450–500).

range 500–1500 m (Fig. 2b) occurs during the uncoupled spinup. As was discussed earlier by Marsland et al. (2003), the model does not adequately simulate the observed northward penetration of Antarctic Intermediate Water (AAIW). However, this appears to be a persistent problem in coarse-resolution ocean models, even those dedicated to AAIW variability investigations (Santoso and England 2004). Over the runtime of the coupled experiment, the salinities in the deep ocean increase further because the deep-water masses produced by the model are too salty and too warm. Errors in the simulated water mass properties could potentially lead to misinterpretations of the THC variability. However, although there is a small trend in the THC time series (see below), the character of the variability does not change over the runtime of the experiment.

The global and Atlantic meridional overturning streamfunctions (Fig. 3) reproduce the well-known features of an upper cell associated with the formation of North Atlantic Deep Water and the surface wind system and a lower cell related to the northward spreading Antarctic Bottom Water. Compared with the uncoupled experiment described in Marsland et al. (2003), the upper cell in the Atlantic is stronger, exceeding 19 Sv (1 Sv = 10^6 m^3 s^{-1}) around 30°N. Furthermore, the zero-contour, separating the large counterrotating cells, lies considerably deeper (3000 m compared to 2200 m). Our results are consistent with the results of observations (e.g., Ganachaud and Wunsch 2000) and other state-of-the-art CGCMs [e.g., Hadley Centre, Gordon et al. 2000; National Center for Atmospheric Research (NCAR), Gent et al. 2002]. In the following, we use the maximum of the streamfunction at 30°N as an index of the strength of the MOC and refer to it as meridional overturning index (MOI). Global and Atlantic poleward heat transports implied by the net surface atmosphere–ocean heat flux (averaged over the years 100–500) are depicted in Figs. 3c,d. For the global ocean, the model compares well with observational estimates (Rintoul and Wunsch 1991; Macdonald and Wunsch 1996; Johns et al. 1997). The heat flux is poleward in both hemispheres, and the maximum northward heat transport amounts to 1.8 PW at 20°N. In the Atlantic, however, the model underestimates the poleward heat transport in the Northern Hemisphere and simulates a maximum of about 0.9 PW at 20°N as opposed to 1–1.2 PW reported from inverse calculations (e.g., Macdonald and Wunsch 1996). The global heat flux imbalance of approximately 0.2 PW reflects the heat taken up by the ocean over the time period of 400 yr that leads to the warming of the intermediate and deep layers of the ocean (Fig. 1). This number should be compared to the upper-ocean (0–750 m) warming rate of 0.29 PW estimated by Willis et al. (2004) for the period from 1993 to 2003 from observations.

The Northern Hemisphere ice thickness fields averaged over the years 100–500 are shown in Fig. 4a for late winter (March) and in Fig. 4b for late summer (September). Compared to ice extent observations (Parkinson et al. 1999), the model-simulated extent ap-

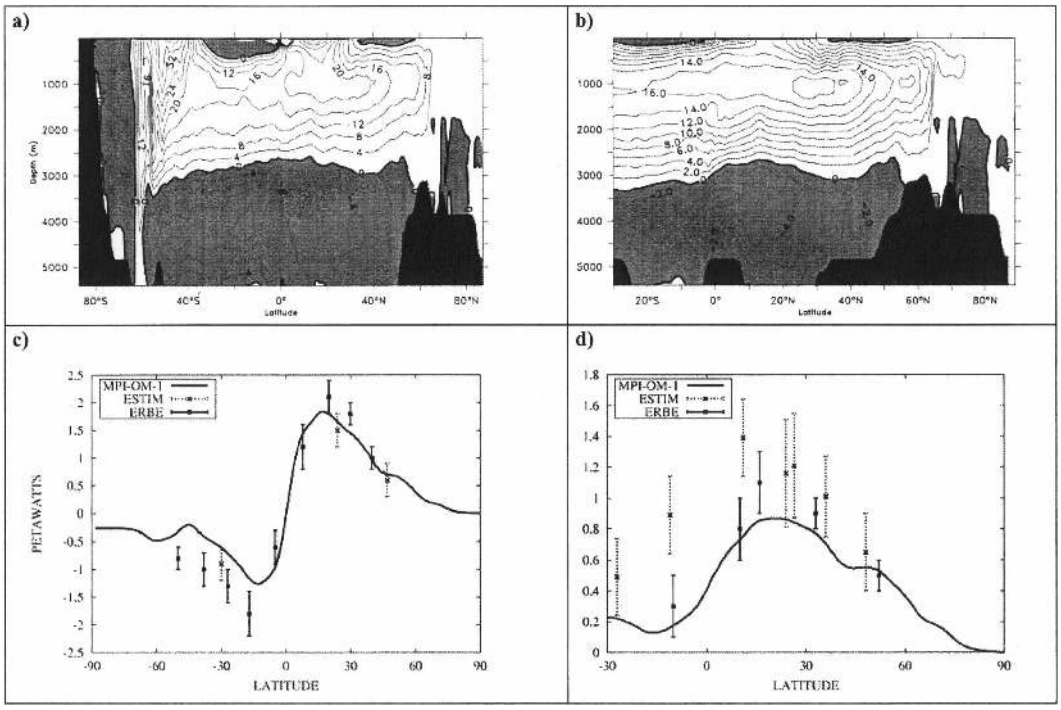

FIG. 3. (a) Global and (b) Atlantic meridional overturning streamfunction [contour interval (c.i.) = 4 and 2 Sv for the global and Atlantic, respectively]; (c) global and (d) Atlantic meridional heat transports (PW) implied by net ocean to atmosphere heat flux. The MPI-OM transports and fluxes are averaged over the years 100–500 of the simulation. Heat transport estimates (ESTIM) with error bars based on observations are taken from Rintoul and Wunsch (1991), Macdonald and Wunsch (1996), and Johns et al. (1997). 1988 estimates derived from the top of the atmosphere as part of the Earth Radiation Budget Experiment (ERBE) and using ECMWF Re-Analysis (ERA) data to remove atmospheric heat transports are taken from Trenberth and Solomon (1994).

pears to be somewhat too large. For example, the ice cover in the Iceland Sea, where sea ice normally reaches the Icelandic coasts only in severe winters, is overestimated. Ice thickness is poorly observed and ice conditions are subject to dramatic changes over multidecadal time scales. Individual measurements, for example from the submarine observations (Rothrock et al. 1999), report ice thickness ranging from 4.2 m (1958–76) to about 2.5 m (1990s). The model-simulated (long-term average) ice thickness in the central Arctic therefore appears to be in this range but slightly too high. The model = simulated Arctic ice volume ($27.6 \pm 1.8 \times 10^3$ km^3) compares, however, well with other coupled models (e.g., Gordon et al. 2000) and regional ice–ocean models (Hilmer and Lemke 2000; Köberle and Gerdes 2003). A climatological freshwater budget of the Arctic Ocean is presented in Table 1. All transports are calculated with respect to a reference salinity of 34.80 (Aagaard and Carmack 1989). The Arctic Ocean receives freshwater mainly from precipitation surplus and river runoff where the latter provides roughly two-thirds of the total nonoceanic input of 4742 km^3 yr^{-1}. Another positive contribution stems from the inflow of relatively fresh Pacific waters through the Bering Strait. Although the mass transport of about 0.7 Sv simulates the observed estimate (0.8 Sv) rather well, the model appears to underestimate the amount of liquid freshwater in comparison with observations. The largest freshwater sink is Fram Strait, through which 3497 km^3 yr^{-1} of freshwater are exported. Roughly two-thirds (2382 km^3 yr^{-1}) of the outflow leaves the Arctic in the form of sea ice. The Fram Strait ice export figures are well in the range of the observational estimates of 2790 (Aagaard and Carmack 1989), 3009 (Vinje et al. 1998), and 2366 km^3 yr^{-1} (Kwok and Rothrock 1999). The simulated transports through the Canadian Archipelago are, however, considerably smaller than the observational estimates. Apparently, the channels and straits are not well enough resolved in our model to allow for a proper simulation of the circulation in this region.

The model's deep-water formation takes place both to the north and to the south of the Greenland–Scotland ridge. Convectively active regions, as indi-

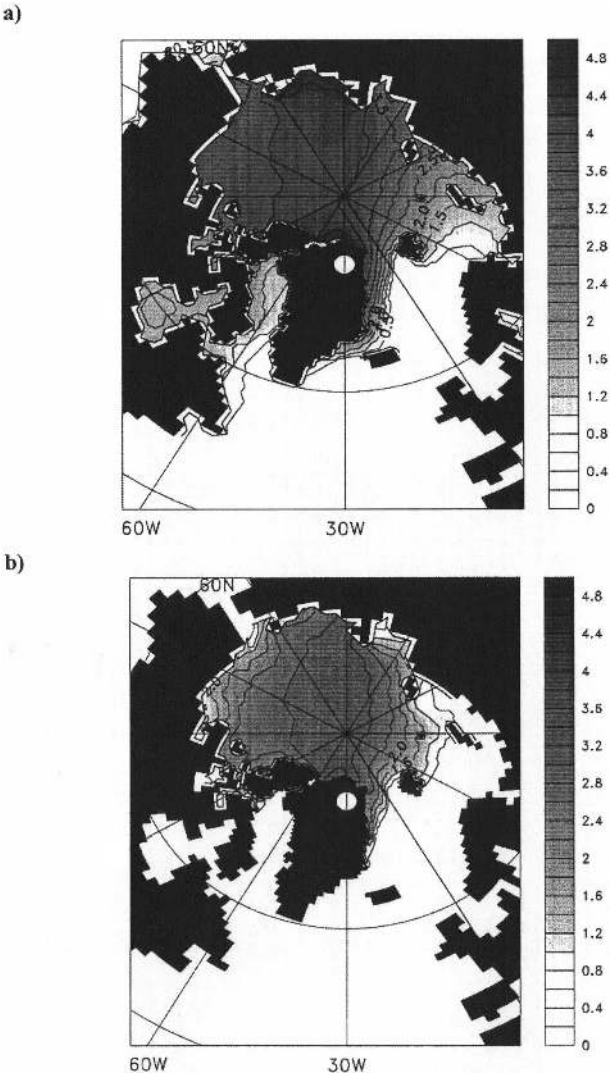

FIG. 4. North Atlantic/Arctic sea ice thickness (m) averaged over the years 100–500 in (a) late winter (Mar) and (b) late summer (Sep); c.i. = 0.5 m, and values exceeding 0.01 m are shaded.

cated by deep mixed layer depths (MLDs; Fig. 5), can be seen in the central Greenland Sea gyre, but also to the south in the Norwegian Sea. There is pronounced variability in the convective activity leading to changes in the spatial distribution of convection sites. South of the Greenland–Scotland Ridge, deep-water renewal takes place in a relatively broad region extending from the LS to about 40°W. The convection region migrates zonally so that it is sometimes concentrated in the LS [as in observations (e.g., Pickart et al. 2002) and in the uncoupled simulation of Marsland et al. (2003)] but often extends too far to the southeast. In the following, however, we shall refer to the convection site to the south of Greenland as LS convection. A relatively broad convection region to the south of Greenland is a common feature of coupled GCMs (DMS93; Timmermann et al. 1998; Holland et al. 2001). Many coarse-resolution models, however, do not simulate convection north of the sill. The deep-water formation in the Nordic Seas is linked to the global thermohaline circulation via the overflows across the Greenland–Scotland Ridge. The relatively dense waters flow through the Denmark Strait and the Faeroe Bank Channel. In the model, overflow transport rates at the sills ($\sigma_\theta > 27.8$) are close to 3 and 2 Sv, respectively, in agreement with observations (Ross 1984; Saunders 1990).

3. Variability

Figure 6a shows time series of the North Atlantic MOI and the northward heat transport at 30°N. Since there is some adjustment during the first decades, we discard all model fields prior to year 100 in the following analysis. A multidecadal variation with a period of approximately 70–80 yr is obvious in the MOI time series. A spectral analysis (Pohlmann et al. 2004) reveals that there is a dominant peak at 70 yr and another

TABLE 1. Freshwater budget for the Arctic Ocean. Units are $km^3\ yr^{-1}$. Freshwater fractions are relative to reference salinity 34.80 (Aagaard and Carmack 1989).

Source	Solid	Liquid	Total	Aagaard and Carmack (1989)
Barents Shelf	−207 ± 121	−467 ± 226	−674	−790 (liquid)
Bering Strait	−445 ± 226	818 ± 226	373	1670 (liquid)
Fram Strait	−2382 ± 506	−1115 ± 311	−3497	−980 (liquid) −2790 (ice)
CAP	−108 ± 42	−668 ± 134	−776	−920 (liquid)
$\delta FW/\delta t$	11 ± 407	−45 ± 561	−34	
$P - E$ + runoff			4659	4200
Freezing and melting	3253 ± 805	−3253 ± 805		

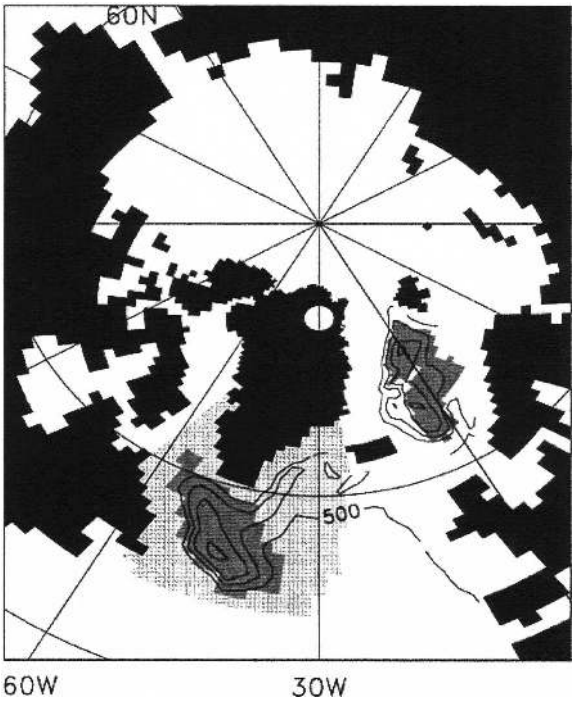

FIG. 5. Late winter (Feb–Mar–Apr) mixed layer depth averaged over the years 100–500 (c.i. = 500 m). The dark gray areas denote the convection regions where the mixed layer depth exceeds 1500 m during at least 10 winters. The cross-hatched area is the northwest Atlantic box used for freshwater and heat budget calculations.

maximum at 100 yr exceeding the 99% confidence level. The peak-to-peak amplitude of the low-pass-filtered overturning index is about 4 Sv, or 20% of the mean. These variations are in phase with fluctuations in the meridional heat transport at 30°N, which attain an amplitude of almost 0.2 PW (Fig. 6a).

Low-frequency variability can also be seen in a number of other fields in the North Atlantic/Arctic region. Latif et al. (2004) have shown that the North Atlantic SST, averaged over the region 40°–60°N, 50°–10°W is proportional to the overturning and may be used as a measure of the MOC. The Arctic ice volume (Fig. 6b) is generally low during times of strong overturning and vice versa. The changes in the ice area, for example, are most pronounced on the Barents Shelf and in the Kara Sea, that is, those regions that are directly influenced by Atlantic waters. Note, however, that the ice volume, not its time derivative or the ice exports are in phase with the THC. The Arctic sea ice appears to act as an integrator of climatic changes associated with the THC where additional feedbacks (Bengtsson et al. 2004) play an active role.

River runoff into the Arctic Ocean is roughly in phase with the MOC with a time lag of a few years (Fig. 6b). The variations of the large-scale precipitation are expected if the oceanic poleward heat transport changes significantly. Warmer North Atlantic SSTs enable higher moisture fluxes toward the Eurasian continent and stronger precipitation in the catchment area of the rivers.

Fluctuations in the intensity of the MOI are related to changes in the density, salinity, and temperature structure of the North Atlantic. In particular, the MOI is closely linked to the LS deep-water formation intensity. Figure 7 depicts normalized time series of the MOI and the late winter (February to April) mixed layer depth averaged over the convection regions in the western North Atlantic (LS) and GS. Here and in the following regression analyses, annual mean data [except for mixed layer depth and sea level pressure (SLP) where the late winter data were taken] from the years 100 to 500 were used and a 21-yr running mean was applied to filter out high-frequency variability. The overturning follows the convection intensity in the Labrador Sea and highest correlation ($r > 0.75$) for lead a lead time of 12 yr. The convection intensities in the Greenland Sea and in the Labrador Sea are out of phase most of the time. The convection intensity is determined by the local stability of the water column and the surface heat fluxes. The relation between the upper-ocean (0–300 m) density in the LS convection region and the MOI is investigated by calculating linear regressions between the respective time series (Fig. 8). The density in the LS convection region leads the MOI by several years, suggesting that density fluctuations precondition the water column and eventually modulate the convection strength. The density time series is decomposed into contributions from temperature and salinity. The salinity anomalies are in phase with the MOI whereas density fluctuations attributable to temperature are opposite in sign and lag by several years. Both components sum up to a density time series that leads the MOI. Although the fluctuations described by DMS93 showed a considerably shorter time scale (about 50 yr), the phase relation between the density constituents and the MOI is remarkably similar (cf. their Fig. 8).

Regressions between the density constituents and the mixed layer depths in the main convection regions show an important difference between the convective regions in the Labrador Sea and in the Greenland Sea (Figs. 8c,d). In both regions, the convection strength is determined by the upper-ocean density, but the positive density anomaly is mainly determined by anomalously salty conditions in the LS (Fig. 8b) and by anomalously cold conditions in the GS (Fig. 8c). We note, however, that, in both regions, the maxima in the density contributions

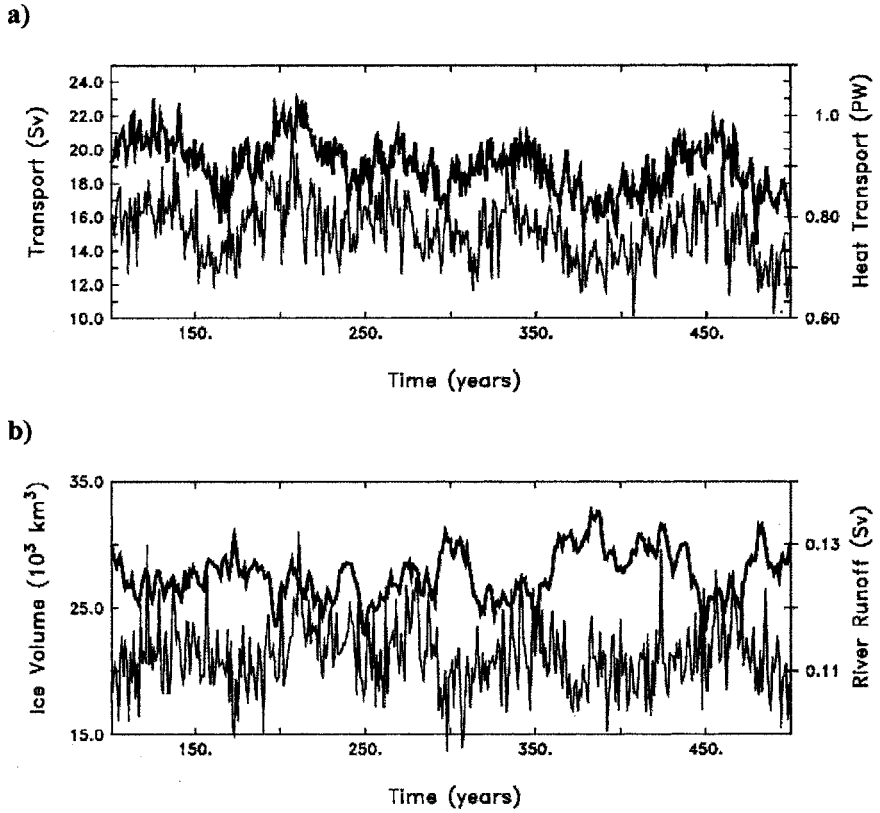

FIG. 6. Time series of (a) the maximum of the MOC at 30°N (thick line; left axis) together with the meridional heat transport at 30°N (thin line; right axis), and (b) the Arctic ice volume together with the river runoff into the Arctic Ocean.

owing to salinity (LS) and temperature (GS) lag the respective density maxima by a few years. It appears that the sign reversal of the density tendency is initiated by a growing contribution from temperature (warming in the LS) and salinity (freshening in the GS). This is important for the phase reversal of the MOI oscillation (Griffies and Tziperman 1995).

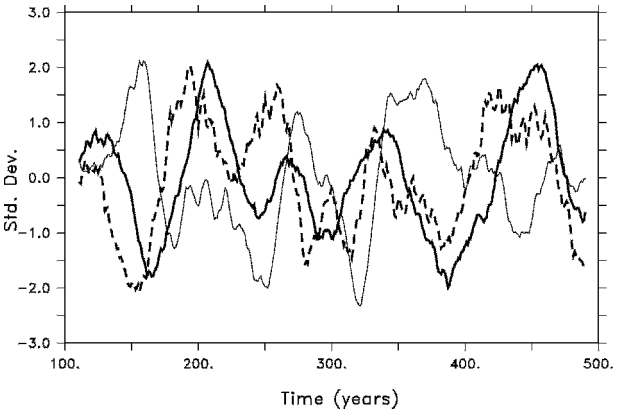

FIG. 7. Normalized time series of the MOI (thick solid line) and the MLD averaged over the convection region south of Greenland (LS; dashed line) and in the GS (thin line).

To further investigate the nature of the fluctuations, linear regressions between the MOI and the two-dimensional fields of upper-ocean (0–300 m) temperature, salinity, and density are computed for various time lags (Fig. 9). Variations in the oceanic heat and salt transports are generally in phase and significantly influence the water mass structure of the upper ocean. Comparing the situation during MOI− (lag −45 yr) and MOI+ (lag 0) reveals that the temperature and salinity anomalies are in phase for the major part of the North Atlantic and the Nordic Seas, that is, the upper-ocean waters are cold and fresh during the low MOI and warm and saline during the high MOI phase. The amplitude of the temperature anomalies is highest in the subpolar gyre and in the Greenland and Norwegian Seas, indicating the influence of the varying heat transport of the Gulf Stream and North Atlantic Drift. However, the central Arctic behaves distinctively different, and this appears to be the key mechanism behind the

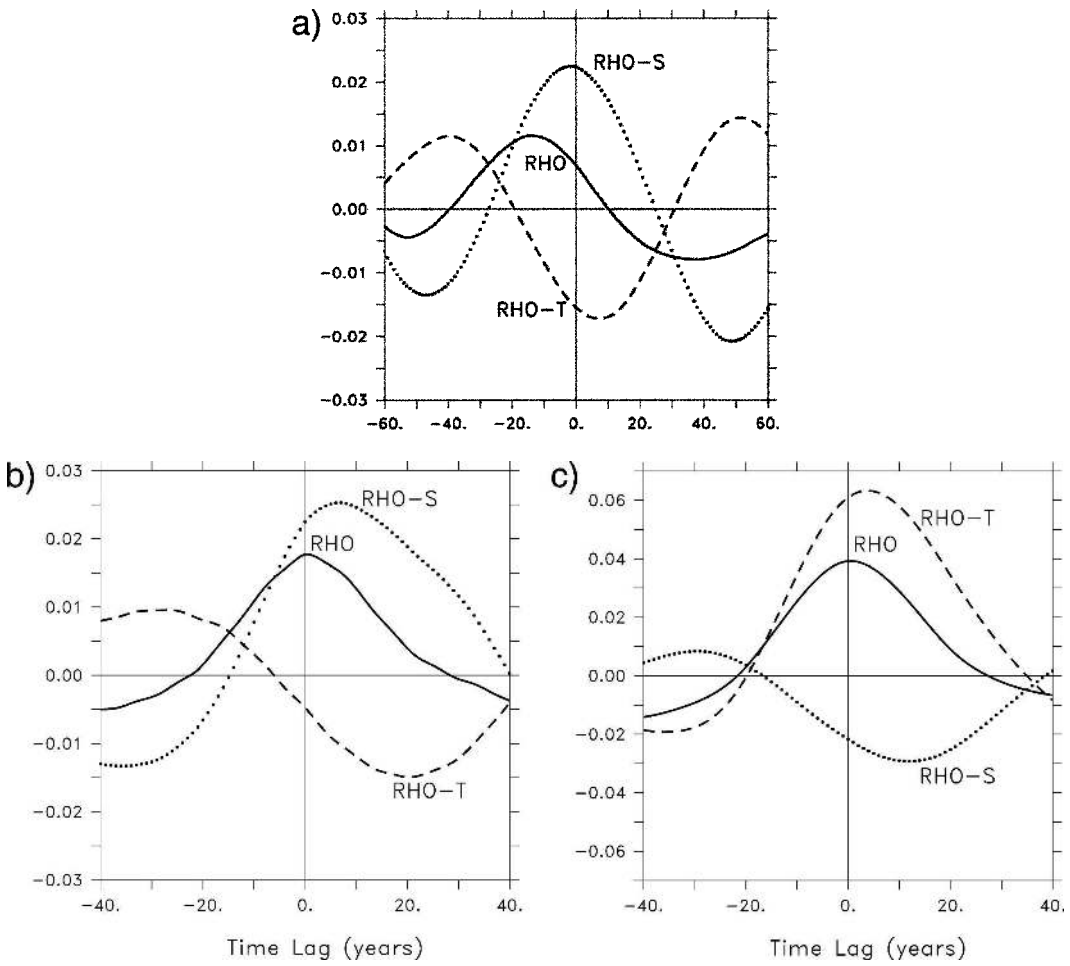

FIG. 8. (a) Regression between the upper-ocean (0–300 m) density averaged over the LS convection region and the MOI. The solid line denotes density anomalies, the dotted line denotes the density anomalies attributable to salinity changes, and the dashed line denotes the density anomalies attributable to temperature changes. Units are kg m^{-3} per standard deviation of the MOI. Regression between the upper-ocean (0–300 m) density averaged over (b) the LS and (c) the GS convection region and the respective MLD time series. Lines are the same as in (a). Units are kg m^{-3} per standard deviation of the MLD.

phase reversal that is necessary to maintain the oscillatory mode. At lag −45 yr, there is a pronounced positive salinity (and density) anomaly centered over the North Pole. At lag −25 yr, the regression suggests that the salinity anomaly has been released from the Arctic, following the Greenland coast southward, and has started to precondition the LS convection region. In the central Arctic, the density anomaly has become negative at lag −15 yr and mirrors the former positive anomaly around the time of maximum overturning (lag 0). Again, as can be seen in the salinity anomaly at lag 25 yr (Fig. 9), the freshwater anomaly is discharged from the Arctic via the East Greenland Current (EGC) acting to increase the stability in the convective region. However, the LS convection site is clearly influenced also by temperature and salinity anomalies from the subpolar gyre.

During the MOI− phase (lag −45 yr), there are pronounced positive density anomalies in the subpolar North Atlantic, the Norwegian and Greenland Seas, and in the central Arctic. These are associated with baroclinic circulation changes that are consistent with the vertically integrated thermal wind relation. Negative anomalies (light conditions) prevail in the Labrador Sea, Iceland Sea, and Barents Sea. It is important to note that the density anomalies are partly attributable to salinity and partly attributable to temperature anomalies. The positive density anomalies are due to

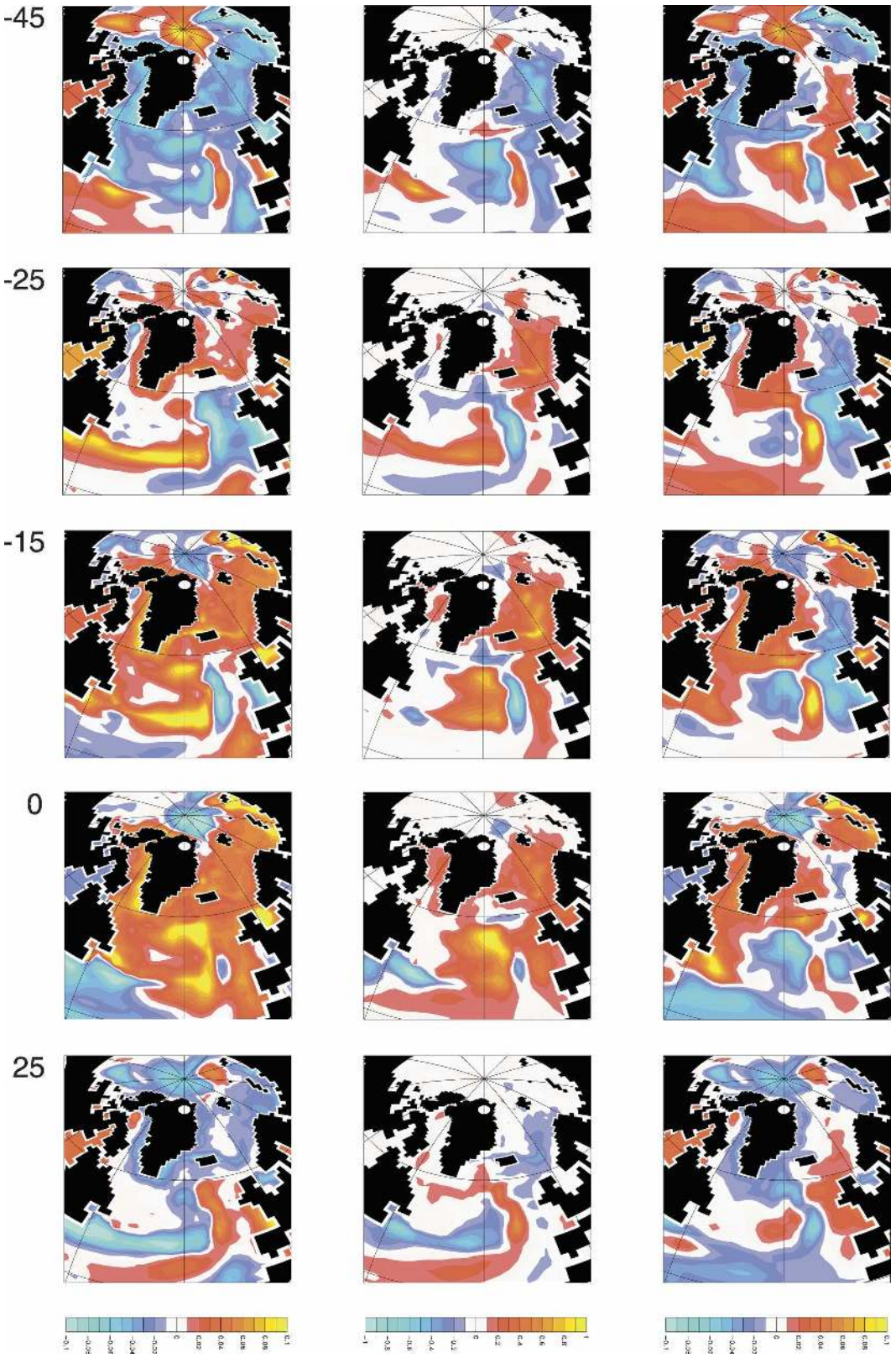

FIG. 9. Regression between the upper-ocean (0–300 m) (left) salinity, (center) temperature, and (right) density and the MOI for time lags −45, −25, −15, 0, and 25 yr. Negative lags refer to the time prior to the MOI maximum. Units are psu, °C, and kg m^{-3} per standard deviation of the MOI time series, respectively.

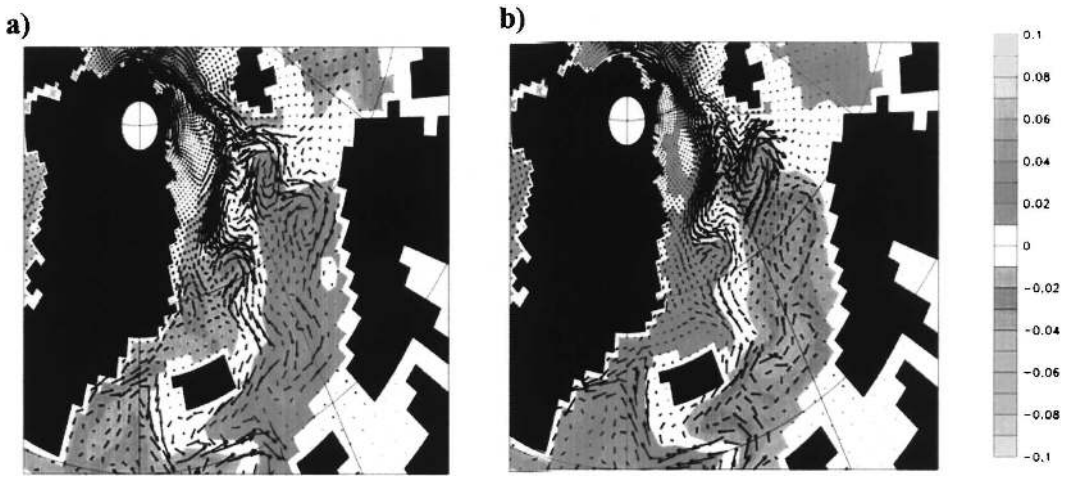

FIG. 10. Regression between the upper-ocean (0–300 m) density and currents and the MOI for time lags (left) −45 and (right) −15 yr. Positive anomalies are shaded dark gray, and negative anomalies are light gray. Negative lags refer to the time prior to the MOI maximum. Units are kg m^{-3} per standard deviation of the MOI time series.

anomalously cold conditions in the subpolar North Atlantic and in the Norwegian and Greenland Seas, but the relatively dense near surface waters in the central Arctic are caused by positive salinity anomalies. Likewise, negative density anomalies in the Iceland Sea and in the Irminger and Labrador Seas are related to fresher than normal conditions. This discrimination is caused by the difference in the relative importance of temperature and salinity in determining the density in the warm water path (North Atlantic Drift) and in the cold water path [EGC and Canadian Archipelago (CAP)], respectively. The positive density anomalies occurring during MOI− in the subpolar North Atlantic are associated with cyclonic circulation anomalies (not shown).

The development of temperature-determined density anomalies and the associated baroclinic circulation changes in the subpolar North Atlantic resemble those in the simulation of DMS93. They describe the phase difference between the overturning (associated with variations in the meridional heat transport) and the gyre circulation (caused by the changes in the upper-ocean temperature and the related geostrophic adjustment) as the key element explaining the interdecadal variations in their model. The zonal transport of salinity with the anomalous (temperature driven) gyre circulation provides the necessary feedback [i.e., when there is a cold (cyclonic) gyre, there is a net westward salt transport to the north of the gyre center that provides the salt necessary to enhance convection]. In our simulation, we see additional baroclinic circulation responses in the Greenland Sea and in the central Arctic (Fig. 10). During the low MOI phase, the Norwegian and Greenland Seas (but not the Iceland Sea) are colder and denser than normal. In addition, the cyclonic circulation anomaly enhances the strength of the Greenland Sea gyre. Therefore the convection is intensified and GS convection appears to be almost out of phase with the overturning strength. Near Fram Strait, the velocity anomalies show that both the East Greenland Current and the West Spitsbergen Current (WSC) are intensified. The accelerated EGC leads to freshwater accumulation in the Iceland Sea and in the basins farther downstream maintaining the relatively stable surface conditions. Since the Arctic loses freshwater with the enhanced EGC and gains salt by the anomalous strong WSC, there is an accumulation of relatively saline waters in the central Arctic. Eventually, the salinity accumulation in the central Arctic makes the Arctic "source" waters of the EGC sufficiently saline to overcome the velocity anomalies in the EGC. In the transition phase at lag −25 yr (Figs. 9), the boundary current along Greenland shows positive salinity anomalies. These increase with time, and at lag −15 yr the density and salinity anomalies are most pronounced preconditioning the peak of LS convection (Fig. 8). At the same time, the increasing heat transports have made the Greenland Sea relatively warm and light so that the circulation anomaly has changed its sign and anticyclonic anomalies have developed (Fig. 10b). In particular, the EGC shows northward current anomalies in the northern Greenland Sea. This inhibits the freshwater transport to the south so that the positive salinity anomalies in the Iceland, Irminger, and Labrador Seas increase, leading to a further intensification of convection in the LS region. The net freshwater export

anomaly out of the Arctic in Fram Strait is now negative (i.e., there is less EGS freshwater export and less saline inflow by the WSC) so that freshwater accumulates in the central Arctic (lag 0 in Fig. 9). Eventually, however, the freshening effect in the source region of the Fram Strait outflow overwhelms the transport anomalies, and positive freshwater anomalies are released through Fram Strait by the mean currents and propagate southward toward the LS convection region (lag 25 in Fig. 9). Now the deep-water formation decreases, and the cycle is closed.

In addition to the freshwater anomalies from the north, the LS convection region is also influenced by density anomalies that originate in the subpolar gyre of the North Atlantic. For example, the positive temperature (negative density) anomalies in the subpolar North Atlantic (Fig. 9, lag 0) warm the near surface layers in the LS and initiate the decrease of convective activity.

To further investigate the origin of the fluctuations and to better understand the relative roles of the Arctic and the North Atlantic contributions, we calculate freshwater and heat budgets for the region of strongest convection in the western North Atlantic. However, we do not use the previously defined convection regions (gray-shaded areas in Fig. 5) but a somewhat larger box (cross-hatched region in Fig. 5) that allows for discrimination between fluxes from the ATL (eastern and southern boundaries), the CAP, and the Denmark Strait (DEN). Surface fluxes of heat and freshwater (precipitation minus evaporation plus runoff) were taken into account. The heat content HC and freshwater storage FWC are defined by

$$\mathrm{HC} = c_p \rho \int_{\text{upper ocean}} (T - T_{\mathrm{ref}})\, dz$$

and

$$\mathrm{FWC} = \int_{\text{upper ocean}} (S - S_{\mathrm{ref}})/S_{\mathrm{ref}}\, dz,$$

where S_{ref} and T_{ref} are the respective reference temperature and salinity, here taken to be $S_{\mathrm{ref}} = 34.95$ and $T_{\mathrm{ref}} = 0°\mathrm{C}$. The budget equations that describe the temporal changes of the storage terms are given by

$$\int\int \mathrm{HC}_t, \quad \int\int \mathrm{FWC}_t = \Sigma(\text{fluxes through boundaries}) + \int\int \text{surface fluxes}.$$

The storage time series and the terms from the budget equation that represent lateral advection are then regressed against the MOI time series. Figures 11a and 11c show the regression between, respectively, the freshwater and heat content and the MOI. Although the integration area is different, the temporal evolution of freshwater and heat content is similar to the upper-ocean density evolution in the more restricted convection region (Fig. 8a). We concentrate on the lateral advective fluxes and have omitted the diffusive terms and the vertical fluxes through the lower boundary of the box at 300 m. The box that we have chosen is influenced by the subpolar gyre (boundary ATL East and ATL South), the East Greenland Current (DEN), and the flows into the Labrador Sea that stem mainly from the CAP. The freshwater content tendency attains its most negative value at lag −22 yr. We note that the amplitude of the tendency term is relatively small compared to the major advective fluxes. At this time, the inflows of relative saline Atlantic waters from the east and the outflow to the south are approximately balanced. The negative tendency is therefore a result of the negative freshwater contribution from the north (DEN) and a positive contribution from the east (CAP) and an additional small negative contribution from downward advection as convection increases (not shown). A further decomposition of the advective transports into contributions from the mean tracer field and the mean velocity field, respectively, revealed that the advective freshwater changes are mainly due to anomalous salinities.

The zero crossing of the tendency terms occurs around the time of maximum MOI when the salinity (Fig. 8a) is highest and the box averaged freshwater content is at a minimum. The East Greenland Current provides a source of anomalously low freshwater during and before the time of strong convection. The increase in the freshwater content thereafter, however, is largely affected by the contributions from the subpolar gyre.

The local surface flux shows negative anomalies in phase with the MOI. These local fluxes enhance the destabilization of the water column and favor convection. Note that the Canadian Archipelago contribution is out of phase with the Denmark Strait fluxes providing positive freshwater anomalies that would tend to damp convection.

For the heat content, we find that the subpolar gyre and, to a lesser degree, the Denmark Strait fluxes provide positive heat content anomalies around the time of maximum overturning. As was shown in Fig. 8b, it is this warming that initially leads to the decrease in surface density just after the time of maximum convection. The tendency term (Fig. 11c) is slightly positive so that the maximum in heat content is reached several years after the maximum in MOI (cf. Fig. 8b). A considerable

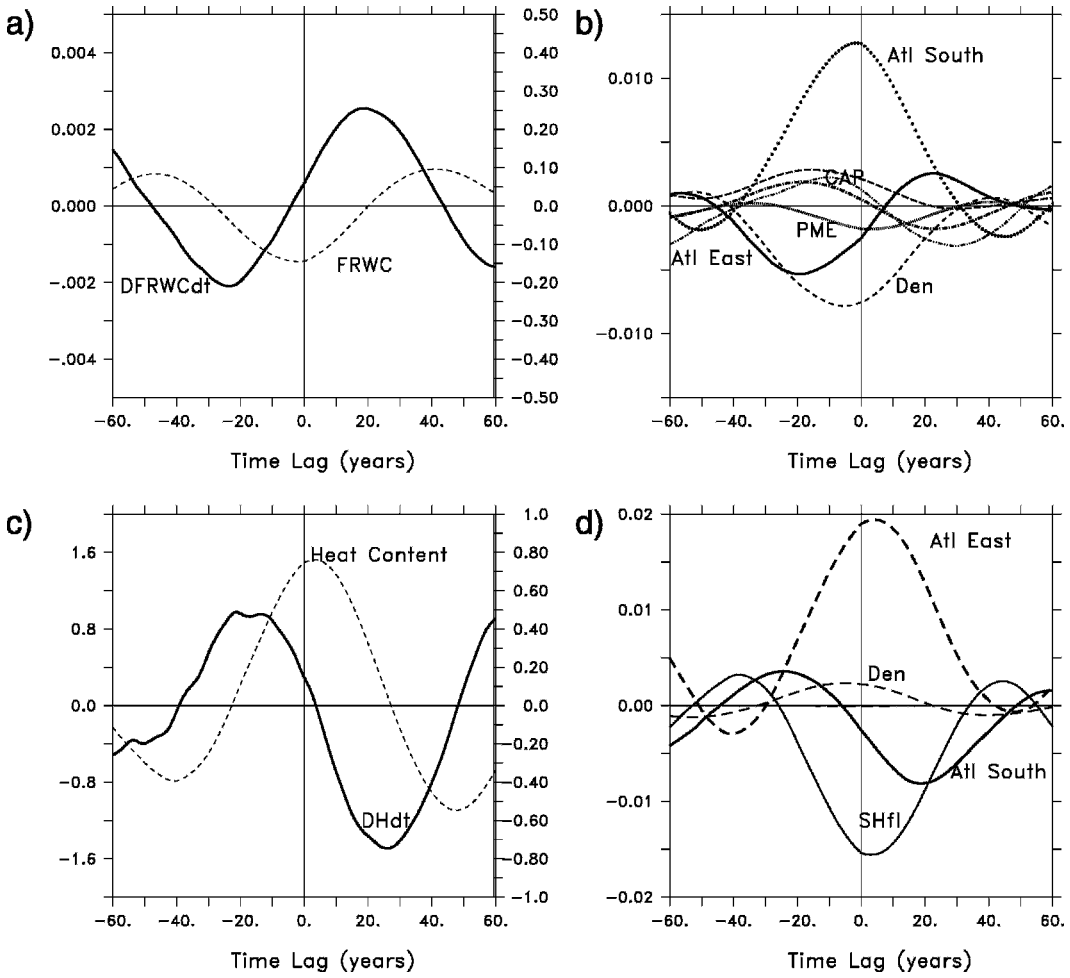

FIG. 11. Regression coefficients between various quantities and the MOI: (a), (b) the freshwater budget equation and (c), (d) the heat budget equation. In (a) the regression between the freshwater storage and the MOI and in (c) the regression between the heat content and the MOI are also given (right axis). Units are Sv per std dev in the MOI for the terms of the freshwater budget, 10^{13} m^3 per MOI std dev for freshwater storage, 10^{12} W per MOI std dev for the terms of the heat budget, and 10^{21} J per MOI std dev for heat content. Labels refer to the boundaries of the cross-hatched box in Fig. 5.

amount of heat is exported from the box by surface fluxes. The minimum in the heat flux term occurs slightly after lag 0 and several years after the convection maximum indicating that the atmosphere damps the SST anomalies that are advected into the region by the subpolar gyre and the East Greenland Current.

We have shown that the hydrographic conditions and the upper-ocean density in the LS convection area are strongly influenced by variations in the EGC freshwater transports. Delworth et al. (1997) found fluctuations in the EGC and suggested that the MOI might be modulated by freshwater of Arctic Origin capping in the LS. In their study, the positive EGC transport anomalies were related to atmospheric variability, in particular to enhanced northerly winds over the Greenland Sea. In our experiments, we do not see evidence for wind and sea level pressure anomalies that would drive an accelerated EGC. In contrast, a regression between the MOI and the sea level pressure (not shown) indicates negative air pressure and cyclonic wind stress anomalies over the Greenland Sea (centered over northern Norway and associated with northerly airflow anomalies over Fram Strait) just during the high MOI phase when the Greenland Sea is relatively warm. Furthermore, there is no significant correlation between the SLP over the central Arctic and the MOI (Pohlmann et al. 2004). We therefore conclude that the circulation anomalies associated with the different phases of the MOI are a geostrophic response to the density anomalies in the Greenland Sea and the Arctic Ocean.

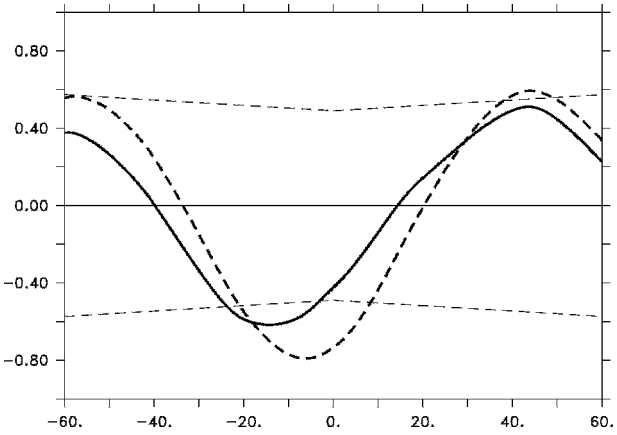

FIG. 12. Lagged correlation between the Fram Strait (thick dashed line) and Denmark Strait (thick line) freshwater transports and the MOI. Thin dashed lines indicate the 95% confidence interval.

Moreover, the EGC current anomalies are not present along the entire east coast of Greenland but occur mostly in the northern Greenland Sea, not in the Iceland Sea and in the Denmark Strait. Nevertheless, both the freshwater transports through the Denmark Strait and Fram Strait are significantly correlated with the MOI, leading the overturning by several years (Fig. 12). This apparent discrepancy can be resolved when the freshwater fluxes are decomposed into contributions by the mean velocity and the mean properties (sea ice and salinity). We find that the advection of anomalous tracers by the mean flow is mainly responsible for the freshwater sensitivity of the MOI in the Denmark Strait, whereas the opposite is true for the Fram Strait (not shown). Therefore, the effect of the EGC anomalies in the Iceland Sea can be seen as an accumulation of positive or negative freshwater anomalies rather than EGC current strength variations. This interpretation is also supported by the difference in the timing of the maximum correlation between the Fram Strait and Denmark Strait in Fig. 12.

To see the difference in the freshwater storage in more detail, composite plots depicting the upper-ocean salinity in the Arctic Ocean for MOI+ (Fig. 13a) and MOI− (Fig. 13b) are shown. Although the Greenland and Barents Seas and even the WSC-dominated region north of Svalbard, Norway are definitively more saline during MOI+ when the Atlantic waters carry additional heat and salt, the central Arctic operates differently. At the North Pole, the upper-ocean salinity differences between MOI+ and MOI− exceed 0.2 psu. Apparently, the Atlantic water tongue originating in the Fram Strait penetrates much deeper into the central Arctic and the Canadian Basin during MOI−. At MOI+, on the other hand, the relatively saline and dense water masses of Atlantic origin in the Barents and Kara Seas are separated from the fresher waters of Pacific and Siberian shelf origin by a pronounced salinity front that runs approximately from the Kara Sea–Laptev Sea boundary to the northeastern tip of Greenland. This front is maintained not only by the anomalous high salinities on the Barents Shelf, but also by an increased transpolar drift transporting freshwater from the Laptev Sea toward the North Pole. During MOI−, however, this front, as can be seen by inspecting the 34.4 isohaline, is deflected toward the North Pole and the upper-ocean currents roughly follow the isohalines geostrophically. The baroclinic circulation anomaly is cyclonic and maintained by relatively dense and saline water in the region between Greenland, Svalbard, and the North Pole (Fig. 13b). The associated upper-ocean current differences between the MOI+ and MOI− phase (Fig. 13c) indicate reduced southward flow in the western part of the Fram Strait and an eastward deflection of the current vectors to the south of Svalbard. Thus the WSC is reduced in favor of a stronger saline flow onto the Barents Shelf. The lack of export and the reduction in the WSC strength lead to the accumulation of freshwater in the central Arctic. The negative density anomaly is further maintained by a transpolar flow along the front above the Lomonossov Ridge. These currents carry extremely fresh waters from the Siberian shelves to the central Arctic.

Since the mean flow along the northern coast of Greenland that finally feeds the EGC is always directed toward Fram Strait (Figs. 13a,b), the negative density anomalies that have been accumulated during the period of reduced Fram Strait freshwater export are eventually advected out of the Arctic and increase the stability in the convectively active region in the Labrador Sea, thus inducing the phase reversal of the MOC strength.

The mechanism described relies mainly on the trapping and release of freshwater in the central Arctic. We have shown in Fig. 6 that there are multidecadal signals in the time series of Arctic ice volume and river runoff. Therefore the question arises of to what extent these important constituents of the Arctic freshwater budget play an active role in the cycle. Changes in the ice volume occur mainly in those areas that are influenced by the heat transport variations arising from the Atlantic. In these areas, in particular the Barents and Kara Shelf, the freshening effect of melting ice is, however, overwhelmed by the increase in salinity due to increased salt transport from the south (Fig. 10). We therefore conclude that melting and freezing of sea ice plays a rather passive role.

Enhanced river runoff occurs almost in phase with

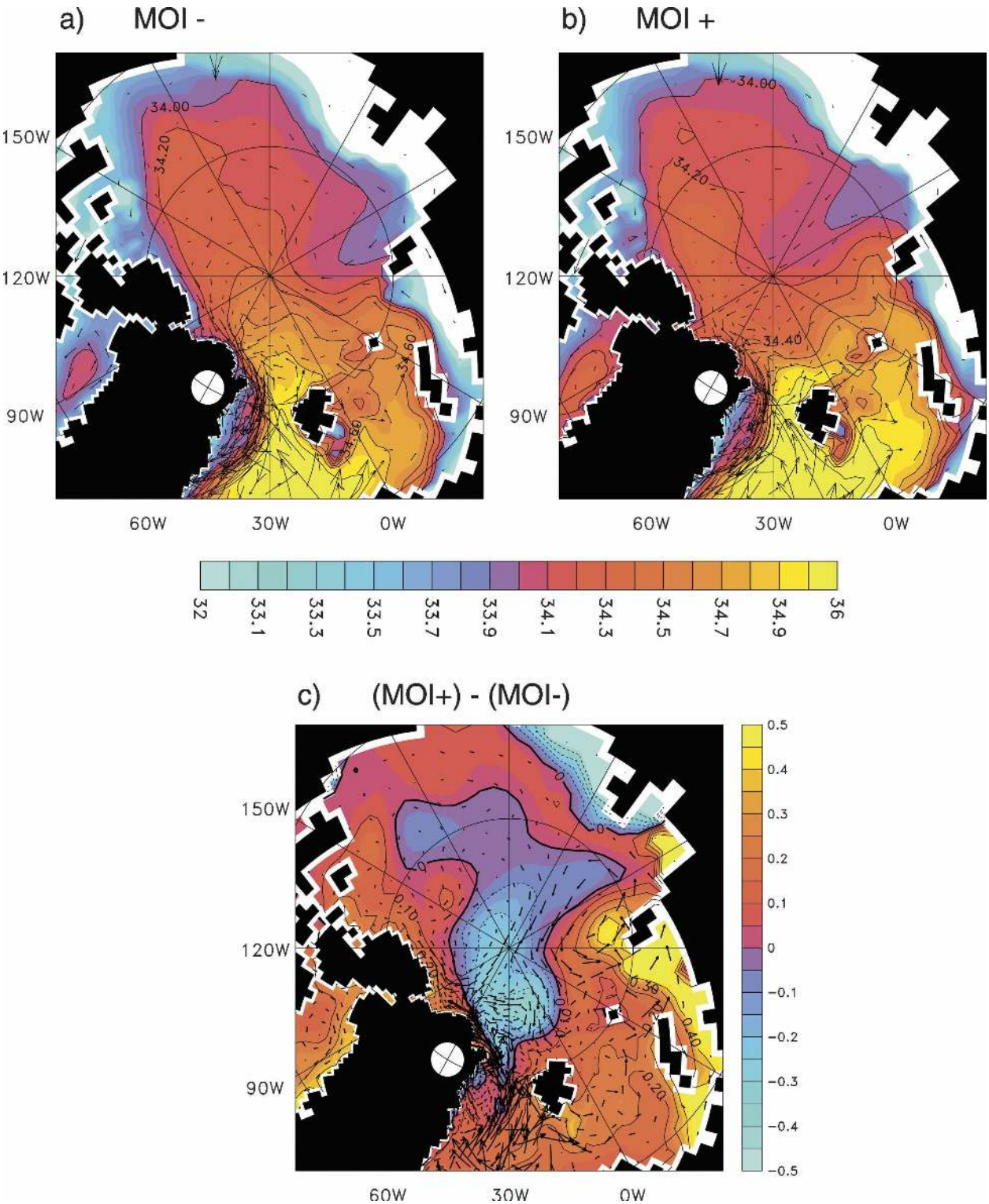

FIG. 13. Composites of the upper-ocean (0–300 m) salinity in the Arctic Ocean and adjacent basins where (a) MOI− represents the situation where the MOC anomaly is less than 1 std dev and (b) MOI+ represents the situation where the MOC anomaly is higher than 1 std dev. (c) The difference between the respective salinity and velocity fields.

the THC with a time lag of a few years when the cyclonic circulation anomaly in the atmosphere that is associated with a warm North Atlantic and increased moisture transport onto the Eurasian continent is fully established. Furthermore, Fig. 13b demonstrates that the variations in the transpolar drift contribute to the accumulation of freshwater just during the MOI+ phase when increasing river runoffs provide additional negative salinity anomalies on the shelves. An intensified hydrological cycle could possibly indicate an ocean–atmosphere–ocean link and thus a coupled mode lack of computer time prevented us from performing additional sensitivity studies with this model. However, in a separate set of experiments with a similar model setup, but with coarser resolution (T31) in the atmosphere and slightly lower resolution (nominal 3°, no equatorial grid refinement) in the ocean, multidecadal variability with similar period and characteristics was diagnosed. The coarse-resolution setup allowed for a number of sensitivity studies to be carried out at moderate costs. Following the approach of Delworth and Greatbatch (2000), we assessed the question of whether the multidecadal variability can be viewed as a coupled air–sea mode. In a series of ocean-only integrations, forced by fluxes extracted from the coupled control run, we found that our model behaves basically the same as the GFDL model. The MOI variability could be reproduced when the fluxes were reapplied to the ocean as they were extracted from the coupled model. The multidecadal variability vanished when a climatological forcing was used but reappeared with somewhat reduced amplitude when the fluxes were applied selected randomly in time. Therefore, the timing of the atmospherically driven freshwater input into the Arctic does not play a significant role. We conclude that the MOI variability arises from a damped mode of the ocean that is continuously excited by the atmosphere.

4. Discussion

We have analyzed the multidecadal variability of the meridional overturning circulation in the coupled AOGCM ECHAM5/MPI-OM. The oscillation is due to a delayed feedback between variations in the meridional overturning and the associated changes in the heat and salt transports and horizontal redistribution of density anomalies. The feedback involves the gyre circulations in the subpolar North Atlantic, the Greenland Sea, and the Arctic Ocean. In particular, we have shown that the storage and release of Arctic freshwater and its control by processes in the Fram Strait are the key mechanisms. The feedback loop can be summarized as follows: We start with increasing salinity and density in the LS convection region and intensified convection. This leads to an intensified overturning and meridional heat transport in the Atlantic. The warming in the subpolar North Atlantic and the Greenland Sea creates pools of relatively light water that are associated with anticyclonic circulation anomalies. These circulation changes and the geopotential height difference between the Greenland Sea and the Arctic Ocean put a control on the freshwater export through the Fram Strait (which is initially a positive feedback, because the accumulation of relative saline waters in the downstream regions of the EGC continues). Eventually, the accumulation of freshwater in the central Arctic reduces the salinity of the EGC source waters to such an extent that the Fram Strait freshwater export anomalies become positive. The freshwater anomalies then reduce the surface density in the LS convection region, and the phase reversal is completed. The inspection of the relative contributions of temperature and salinity to the surface density in the convection regions (Figs. 8b,c) points to important contributions from two side loops: First, positive temperature anomalies in the subpolar North Atlantic propagate westward into the LS convection region and initiate the decay of convection. Second, in a similar manner, negative salinity anomalies in the EGC and in the Iceland Sea are advected into the Greenland Sea gyre and influence the convective activity there.

Although there are important differences, such as the role of the Greenland Sea gyre and the Arctic Ocean, between this simulation and the studies by DMS93, the main mechanism of a damped oceanic mode, continuously excited by the atmosphere, appears to be similar. In particular, there is little evidence for coupled feedbacks. Although our experiments show a more complex spatial structure, we can generally confirm the conclusion of Te Raa and Dijkstra (2002): the fundamental process is the phase difference between variations in the meridional overturning and its associated heat and salt transport and a zonal redistribution of density anomalies. (Huck et al. 2001) report that the oscillation in their model appears to be quite robust to various physical settings, but some effects, such as topography and wind forcing, have a damping role. Therefore the oscillation might decay under constant forcing but would be sustained by the stochastic forcing of the atmosphere. The period of the oscillation will largely be determined by the storage and release time of the gyres (Weaver and Sarachik 1991; Stocker 1996). In particular, the storage and release of freshwater from the central Arctic appears to be a key mechanism. In our simulation, the relatively high resolution in the regions surrounding Greenland allowed for a proper represen-

tation of the exchange flow through the Fram Strait and the frontal region between the Arctic water masses of Atlantic, Pacific, and continental shelf origin. Therefore, although the general mechanism is similar to what was found in previous studies and simplified models, the more detailed representation of convective and frontal processes not only leads to an improvement in the mean state, but also introduces new mechanisms determining multidecadal variability in large-scale ocean circulation.

Whether or not the simulated mechanism is a robust feature of the real North Atlantic–Arctic climate system remains to be verified. Clearly, the multidecadal (50–90 yr) time scale is apparent in a number of observed variables, such as North Atlantic SST (Delworth and Mann 2000; Latif et al. 2004), Arctic sea ice and surface air temperature (Polyakov et al. 2002), and the Fram Strait sea ice export (Schmith and Hansen 2003). Polyakov and Johnson (2000) have linked the low-frequency oscillation with changes in the Atlantic heat transports and thus the thermohaline circulation. On the other hand, the long-term coordinated changes in the North Atlantic and Arctic have been associated with the low-frequency evolution of the NAO during the twentieth century (Dickson et al. 2000). The opposing trends in the Labrador Sea and Greenland Sea convection activity, for example, can be explained by the changing atmospheric circulation patterns. In addition, analysis of the ocean gyre circulation from hydrographic observations (Curry and McCartney 2001) and from hindcast simulations with ocean models forced by National Centers for Environmental Prediction (NCEP) fields (e.g., Haak et al. 2003) suggest that the MOC appears to be modulated by the NAO. In our multicentury integration, the NAO time series has, in contrast to the MOI, no significant peak at multidecadal time scales (Pohlmann et al. 2004). A direct comparison indicates that the time series are not well correlated. However, there are indeed phases (not shown) where long-term trends coincide in both time series. At present, we can neither decide how representative the simulated variability is for the real climate nor decide how anomalous the twentieth-century development of the NAO is for the long-term climate record. A nearly 300-yr-long NAO index reconstructed from tree rings (Fig. 35 of Dickson et al. 1996) shows little sign of a 70-yr period before 1870. Ultimately, the relative roles of the atmosphere and the ocean in changing the North Atlantic and Arctic climate could be clarified by realistic hindcast simulations of the twentieth-century climate with coupled AOGCMs. A first step toward this goal and the required degree of realism has been achieved by Wu et al. (2004). The authors have shown that they were able to reproduce the observed freshening of the deep outflows from the GIN Seas in ensemble simulations with the Hadley Centre climate model. Nevertheless, in parallel with high-resolution experiments, process and sensitivity studies will be necessary to understand the role of individual mechanisms, such as preconditioning and timing of convection, or the overflows.

Acknowledgments. This work was supported by the German Ministry for Education and Research (BMBF) projects CLIVAR Marin (03F0377F) and DEKLIM.

REFERENCES

Aagaard, K., and E. C. Carmack, 1989: The role of sea ice and other fresh water in the Arctic circulation. *J. Geophys. Res.,* **94,** 14 485–14 498.

Belkin, I. M., S. Levitus, J. I. Antonov, and S.-A. Malmberg, 1998: "Great Salinity Anomalies" in the North Atlantic. *Progress in Oceanography,* Vol. 41, Pergamon, 1–68.

Bengtsson, L., V. A. Semenov, and O. M. Johannessen, 2004: The early twentieth-century warming in the Arctic—A possible mechanism. *J. Climate,* **17,** 4045–4057.

Broecker, W. S., 1997: Thermohaline circulation, the Achilles heel of our climate system: Will man-made CO_2 upset the current balance? *Science,* **278,** 1582–1588.

Curry, R. G., and M. S. McCartney, 2001: Ocean gyre circulation changes associated with the North Atlantic Oscillation. *J. Phys. Oceanogr.,* **31,** 3374–3400.

——, ——, and T. M. Joyce, 1998: Oceanic transport of subpolar climate signals to mid-depth subtropical waters. *Nature,* **391,** 575–577.

Delworth, T. L., and R. J. Greatbatch, 2000: Multidecadal thermohaline circulation variability driven by atmospheric surface flux forcing. *J. Climate,* **13,** 1481–1495.

——, and M. E. Mann, 2000: Observed and simulated multidecadal variability in the Northern Hemisphere. *Climate Dyn.,* **16,** 661–676.

——, S. Manabe, and R. J. Stouffer, 1993: Interdecadal variations of the thermohaline circulation in a coupled ocean–atmosphere model. *J. Climate,* **6,** 1993–2011.

——, ——, and ——, 1997: Multidecadal climate variability in the Greenland Sea and surrounding regions: A coupled model simulation. *Geophys. Res. Lett.,* **24,** 257–260.

Dickson, R. R., J. Meincke, S.-A. Malmberg, and A. J. Lee, 1988: The "Great Salinity Anomaly" in the northern North Atlantic, 1968–1982. *Progress in Oceanography,* Vol. 20, Pergamon, 103–151.

——, J. Lazier, J. Meincke, P. Rhines, and J. Swift, 1996: Long-term coordinated changes in the convective activity of the North Atlantic. *Progress in Oceanography,* Vol. 38, Pergamon, 241–295.

——, and Coauthors, 2000: The Arctic response to the North Atlantic Oscillation. *J. Climate,* **13,** 2671–2696.

Folland, C. K., D. E. Parker, and F. E. Kates, 1984: Worldwide marine temperature fluctuations 1856–1981. *Nature,* **310,** 670–673.

——, ——, A. W. Coleman, and R. Washington, 1999: Large scale modes of ocean surface temperature since the late nineteenth century. *Beyond El Niño,* A. Navarra, Ed., Springer, 73–102.

Ganachaud, A., and C. Wunsch, 2000: Improved estimates of global ocean circulation, heat transport and mixing from hydrographic data. *Nature,* **408,** 453–456.

Gent, P. R., J. Willebrand, T. McDougall, and J. C. McWilliams, 1995: Parameterizing eddy-induced tracer transports in ocean circulation models. *J. Phys. Oceanogr.,* **25,** 463–474.

——, A. P. Craig, C. M. Bitz, and J. W. Weatherly, 2002: Parameterization improvements in an eddy-permitting ocean model for climate. *J. Climate,* **15,** 1447–1459.

Gordon, C., C. Cooper, C. Senior, H. Banks, J. M. Gregory, T. C. Johns, J. F. B. Mitchell, and R. Wood, 2000: Simulation of SST, sea ice extent and ocean heat transports in a coupled model without flux adjustments. *Climate Dyn.,* **16,** 147–168.

Griffies, S. M., 1998: The Gent–McWilliams skew flux. *J. Phys. Oceanogr.,* **28,** 831–841.

——, and E. Tziperman, 1995: A linear thermohaline oscillator driven by stochastic atmospheric forcing. *J. Climate,* **8,** 2440–2453.

Haak, H., J. Jungclaus, U. Mikolajewicz, and M. Latif, 2003: Formation and propagation of great salinity anomalies. *Geophys. Res. Lett.,* **30,** 1473, doi:10.1029/2003GL017065.

Häkkinen, S., 1999: A simulation of the thermohaline effects of a Great Salinity Anomaly. *J. Climate,* **12,** 1781–1795.

Hibler, W. D., III, 1979: A dynamic thermodynamic sea ice model. *J. Phys. Oceanogr.,* **9,** 815–846.

Hilmer, M., and P. Lemke, 2000: On the decrease of Arctic sea ice volume. *Geophys. Res. Lett.,* **27,** 3751–3754.

Holland, M. M., C. M. Bitz, M. Eby, and A. J. Weaver, 2001: The role of ice–ocean interactions in the variability of the North Atlantic thermohaline circulation. *J. Climate,* **14,** 656–675.

Houghton, J. T., Y. Ding, D. J. Griggs, M. Noguer, P. J. van der Linden, X. Dai, K. Maskell, and C. A. Johnson, Eds., 2001: *Climate Change 2001: The Scientific Basis*. Cambridge University Press, 881 pp.

Huck, T., A. Colin de Verdière, and A. Weaver, 1999: Interdecadal variability of the thermohaline circulation in box-ocean models forced by fixed surface fluxes. *J. Phys. Oceanogr.,* **29,** 865–892.

——, G. K. Vallis, and A. Colin de Verdière, 2001: On the robustness of interdecadal modes of the thermohaline circulation. *J. Climate,* **14,** 940–963.

Johns, W. E., T. N. Lee, R. J. Zantopp, and E. Fillenbaum, 1997: Updated transatlantic heat flux at 26.5N. *International WOCE Newsletter,* No. 27, WOCE International Project Office, Southampton, United Kingdom, 15–22.

Köberle, C., and R. Gerdes, 2003: Mechanisms determining the variability of Arctic sea ice conditions and export. *J. Climate,* **16,** 2843–2859.

Kwok, R., and D. A. Rothrock, 1999: Variability of Fram Strait ice flux and North Atlantic Oscillation. *J. Geophys. Res.,* **104** (C3), 5177–5189.

Latif, M., and Coauthors, 2004: Reconstructing, monitoring, and predicting decadal-scale changes in the North Atlantic thermohaline circulation with sea surface temperature. *J. Climate,* **17,** 1605–1614.

Levitus, S., and Coauthors, 1998: *Introduction.* Vol. 1, *World Ocean Atlas 1998,* NOAA Atlas NESDIS 18, 346 pp.

Macdonald, A. M., and C. Wunsch, 1996: Oceanic estimates of global ocean heat transport. *International WOCE Newsletter,* No. 24, WOCE International Project Office, Southampton, United Kingdom, 5–6.

Maier-Reimer, E., and U. Mikolajewicz, 1989: Experiments with an OGCM on the cause of the Younger Dryas. *Oceanography 1988,* A. Ayala-Castanares, W. Wooster, and A. Yanez-Arancibia, Eds., UNAM Press, 87–99.

Mann, M. E., R. S. Bradley, and M. K. Hughes, 1998: Global-scale temperature patterns and climate forcing over the past six centuries. *Nature,* **392,** 779–787.

——, ——, and ——, 1999: Northern Hemisphere temperatures during the past millennium: Inferences, uncertainties, and limitations. *Geophys. Res. Lett.,* **26,** 759–762.

Marotzke, J., and P. H. Stone, 1995: Atmospheric transports, the thermohaline circulation, and flux adjustment in a simple coupled model. *J. Phys. Oceanogr.,* **25,** 1350–1364.

Marsland, S. J., H. Haak, J. H. Jungclaus, M. Latif, and F. Röske, 2003: The Max-Planck-Institute global ocean/sea ice model with orthogonal curvilinear coordinates. *Ocean Modell.,* **5,** 91–127.

Pacanowski, R. C., and S. G. H. Philander, 1981: Parameterization of vertical mixing in numerical models of tropical oceans. *J. Phys. Oceanogr.,* **11,** 1443–1451.

Parkinson, C. L., D. J. Cavalieri, P. Gloersen, H. J. Zwally, and J. C. Comiso, 1999: Arctic sea ice extents, areas, and trends, 1978–1996. *J. Geophys. Res.,* **104,** 20 837–20 856.

Pickart, R. S., D. T. Torres, and R. A. Clarke, 2002: Hydrography of the Labrador Sea during active convection. *J. Phys. Oceanogr.,* **32,** 428–457.

Pohlmann, H., M. Botzet, M. Latif, M. Wild, and P. Tschuck, 2004: Estimating the long-term predictability potential of a coupled AOGCM. *J. Climate,* **17,** 4463–4472.

Polyakov, I. V., and M. A. Johnson, 2000: Arctic decadal and interdecadal variability. *Geophys. Res. Lett.,* **27,** 4097–4100.

——, and Coauthors, 2002: Observationally based assessment of polar amplification of global warming. *Geophys. Res. Lett.,* **29,** 1878, doi:10.1029/2001GL011111.

Rintoul, S. R., and C. Wunsch, 1991: Mass, heat, oxygen and nutrient fluxes and budgets in the North Atlantic Ocean. *Deep-Sea Res.,* **38** (Suppl.), S355–S377.

Roeckner, E., and Coauthors, 2003: The atmospheric general circulation model ECHAM5, Part I: Model description. Max-Planck-Institut für Meteorologie Rep. 349, 127 pp.

Röske, F., 2001: An atlas of surface fluxes based on the ECMWF Re-analysis—A climatological dataset to force global ocean circulation models. Max-Planck-Institut für Meteorologie Rep. 323, Hamburg, Germany, 31 pp.

Ross, C. K., 1984: Temperature-salinity characteristics of the "overflow" water in Denmark Strait during "Overflow '73." *Rapp. P. V. Reun. Cons. Int. Explor. Mer,* **185,** 111–119.

Rothrock, D. A., Y. Yu, and G. A. Maykut, 1999: Thinning of the Arctic sea-ice cover. *Geophys. Res. Lett.,* **26,** 3469–3472.

Santoso, A., and M. H. England, 2004: Antarctic Intermediate Water circulation and variability in a coupled model. *J. Phys. Oceanogr.,* **34,** 2160–2179.

Saunders, P., 1990: Cold outflow from the Faroe Bank Channel. *J. Phys. Oceanogr.,* **20,** 29–43.

Schiller, A., U. Mikolajewicz, and R. Voss, 1997: The stability of the North Atlantic thermohaline circulation in a coupled ocean–atmosphere general circulation model. *Climate Dyn.,* **13,** 325–347.

Schmith, T., and C. Hansen, 2003: Fram Strait ice export during the nineteenth and twentieth centuries: Evidence for multidecadal variability. *J. Climate,* **16,** 2782–2791.

Schulz, J.-P., L. Dümenil, and J. Polcher, 2001: On the land surface–atmosphere coupling and its impact in a single-column atmospheric model. *J. Appl. Meteor.,* **40,** 642–663.

Stocker, T. F., 1996: An overview of century time-scale variability in the climate system: Observation and models. *Decadal Climate Variability: Dynamics and Predictability,* L. T. Anderson and J. Willebrand, Eds., Global Environmental Change, NATO ASI Series I, Vol. 44, Springer, 379–406.

Sweby, P., 1984: High resolution schemes using flux limiters for hyperbolic conservation laws. *SIAM J. Numer. Anal.,* **21,** 995–1011.

Te Raa, L. A., and H. A. Dijkstra, 2002: Instability of the thermohaline circulation on interdecadal timescales. *J. Phys. Oceanogr.,* **32,** 138–160.

——, and ——, 2003: Sensitivity of North Atlantic multidecadal variability to freshwater flux forcing. *J. Climate,* **16,** 2586–2601.

Terray, L., S. Valcke, and A. Piacentini, 1998: OASIS 2.2, ocean atmosphere sea ice soil user's guide and reference manual. Tech. Rep. TR/CGMC/98-05, Centre Européen de Recherche et de Formation en Calcul Scientifique Avancé (CERFACS), Toulouse, France, 77 pp.

Timmermann, A., M. Latif, R. Voss, and A. Grötzner, 1998: Northern Hemisphere interdecadal variability: A coupled air–sea mode. *J. Climate,* **11,** 1906–1931.

Trenberth, K. E., and A. Solomon, 1994: The global heat balance: Heat transports in the atmosphere and ocean. *Climate Dyn.,* **10,** 107–137.

Vinje, T., N. Nordlund, and Å. Kvambeck, 1998: Monitoring ice thickness in Fram Strait. *J. Geophys. Res.,* **103,** 10 437–10 449.

Weaver, A. J., and E. S. Sarachik, 1991: Evidence for decadal variability in an ocean general circulation model: An advective mechanism. *Atmos.–Ocean,* **29,** 197–231.

Willis, J. K., D. Roemmich, and B. Cornuelle, 2004: Interannual variability in upper ocean heat content, temperature, and thermosteric expansion on global scales. *J. Geophys. Res.,* **109,** C12036, doi:10.1029/2003JC002260.

Wu, P., and C. Gordon, 2002: Oceanic influence on North Atlantic climate variability. *J. Climate,* **15,** 1911–1925.

——, R. Wood, and P. Stott, 2004: Does the recent freshening trend in the North Atlantic indicate a weakening trend in the thermohaline circulation? *Geophys. Res. Lett.,* **31,** L02301, doi:10.1029/2003GL018584.